Patch-Level Glioblastoma Subregion Classification with a Contrastive Learning-Based Encoder*

Juexin Zhang[†] , Qifeng Zhong[†] , Ying Weng , and Ke Chen

University of Nottingham Ningbo China, Ningbo 315100, China {juexin.zhang,qifeng.zhong,ying.weng,ke.chen2}@nottingham.edu.cn

Abstract. The significant molecular and pathological heterogeneity of glioblastoma, an aggressive brain tumor, complicates diagnosis and patient stratification. While traditional histopathological assessment remains the standard, deep learning offers a promising path toward objective and automated analysis of whole slide images. For the BraTS-Path 2025 Challenge, we developed a method that fine-tunes a pre-trained Vision Transformer (ViT) encoder with a dedicated classification head on the official training dataset. Our model's performance on the online validation set, evaluated via the Synapse platform, yielded a Matthews Correlation Coefficient (MCC) of 0.7064 and an F1-score of 0.7676. On the final test set, the model achieved an MCC of 0.6509 and an F1-score of 0.5330, which secured our team second place in the BraTS-Pathology 2025 Challenge. Our results establish a solid baseline for ViT-based histopathological analysis, and future efforts will focus on bridging the performance gap observed on the unseen validation data.

Keywords: Deep learning \cdot Digital Pathology \cdot BraTS 2025 \cdot Glioblastoma.

1 Introduction

Glioblastoma is a highly aggressive primary brain tumor associated with poor patient outcomes, which makes accurate diagnosis and prognostic assessment critical for guiding therapy [12]. One of the main challenges lies in the marked histopathological heterogeneity of these tumors. Such heterogeneity is evident both across patients (inter-tumoral) and within individual tumors (intra-tumoral) and is reflected in differences in cellular morphology, phenotypic profiles, and treatment responses [9], thereby complicating prognostic evaluation.

Glioblastoma is an aggressive primary brain tumor associated with poor patient outcomes, which makes accurate diagnosis and prognostic prediction critical for guiding therapy [12]. The main challenge lies in the marked histopathological

 $^{^\}star$ Corresponding author: Ying Weng. † Juexin Zhang and Qifeng Zhong contributed euqally to this work.

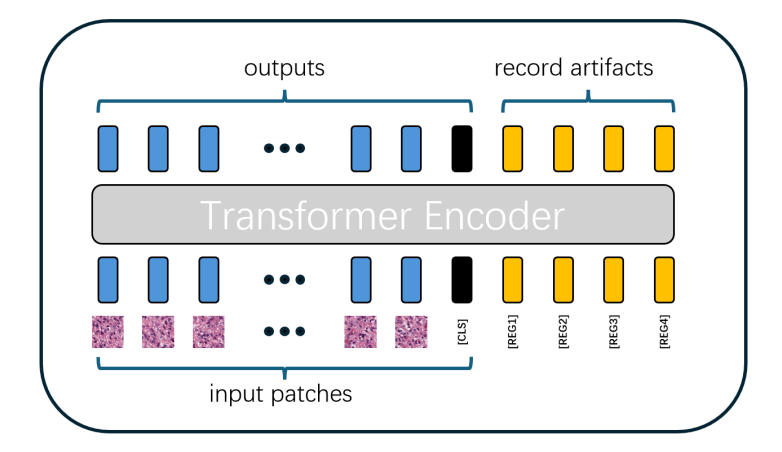


Fig. 1. Virchow2 uses four registers to mitigate local information loss and enhance global contextual information by storing artifact tokens, thereby enabling better feature extraction. Adapted from [2].

heterogeneity of these tumors. This diversity exists both between patients (intertumoral) and within a single tumor (intra-tumoral), manifesting as variations in cellular morphology, phenotypic expression, and therapeutic response [9], which makes the prognosis more complicated.

The diagnosis of brain tumors has usually relied on pathology, where tissue samples are examined under a microscope to get subtypes of tumors and give treatment plans. In recent years, this traditional workflow has been reshaped by the rise of digital pathology, which replaces glass slides with high-resolution digital images of tissue sections. With the development of computational tools, digital pathology is redefining how brain tumors are studied and classified. The availability of whole-slide imaging also opens the door to artificial intelligence methods, especially deep learning models such as convolutional neural networks, which can detect subtle histological features and support faster, more accurate diagnoses.

Building upon this progress, large-scale foundation models pretrained on histopathology data, such as CTransPath [11] and Virchow [13]. As reported by Neidlinger et al. [7], Virchow excels at extracting fine-grained features and outperforms many alternatives. We use the pretrained Virchow2 as a feature extraction backbone, leveraging its ability to capture discriminative tile-level features. For classification, we attach a head consisting of two linear layers to predict the class of each sub-region patch.

2 Methods

For our study, we selected Virchow2 [13] as the foundational pretrained model, chosen for its state-of-the-art performance in computational pathology. The ar-

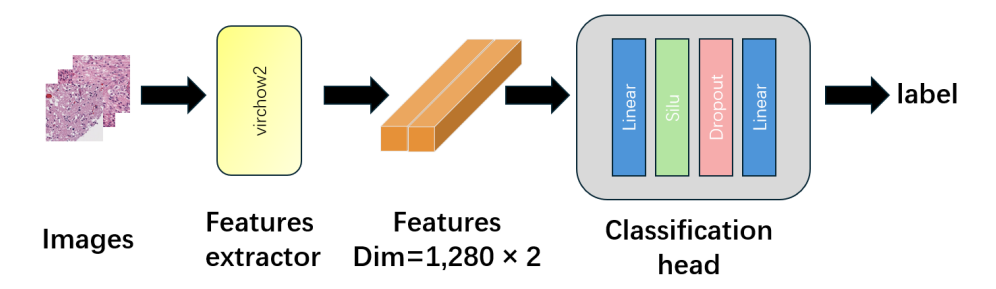


Fig. 2. The network architecture of our model.

chitecture of Virchow2 is built upon the powerful Vision Transformer (ViT-H/14) [3], a high-capacity model known for its ability to capture complex spatial relationships in image data, as illustrated in Figure 1. The power of Virchow2 stems from its extensive pretraining on a massive and diverse dataset comprising approximately 3.1 million whole slide images (WSIs) from over 225,000 patients. This dataset provides comprehensive coverage of nearly 200 tissue types and multiple staining modalities, including the widely used hematoxylin and eosin (H&E) as well as various immunohistochemical (IHC) stains. This robust pretraining ensures the model learns a rich hierarchy of generalizable features relevant to histopathology. Virchow2's feature representation capabilities were developed using DINOv2 [8], a sophisticated self-supervised learning framework. This approach enables the model to learn meaningful features directly from unlabeled images without requiring manual annotations.

To tailor the pretrained Virchow2 for our specific 9-class sub-region classification task, we replace the original classification head with a new one, as depicted in Figure 2. Our approach is designed to create a highly informative feature representation from each input patch before classification. The process begins by dividing each input patch into 256 non-overlapping tiles. These tiles are processed by the Virchow2 encoder, which generates 256 corresponding feature tokens, each with a dimensionality of 1280. To create a comprehensive feature representation for the entire patch, we combine two distinct signals:

- Global Average Representation: We compute the mean of all 256 tokens to produce a single 1 × 1280 vector. This provides a global summary of the patch's overall texture, cellularity, and morphology.
- Semantic Class Token: We also retain the original class token (1×1280) , which the Vision Transformer learns to use as an aggregate representation of the most critical semantic information in the image.

The averaged feature token and the class token are concatenated and flattened to form a final, rich feature vector of size 2560. This dual-representation strategy ensures our classifier has access to both a holistic summary and the most salient features identified by the transformer. This combined feature vec-

4 J. Zhang et al.

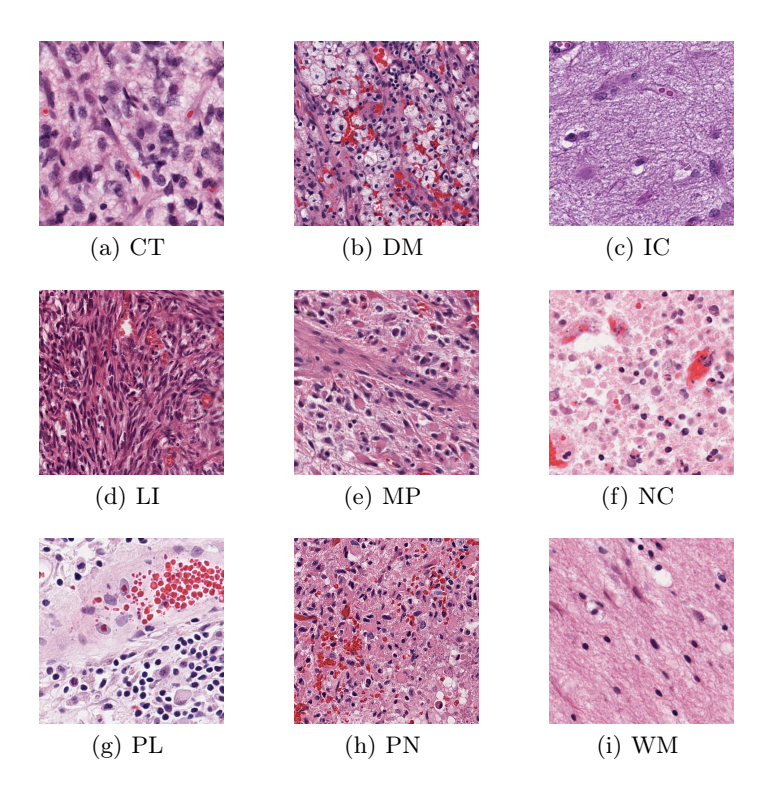


Fig. 3. Illustration of the annotated histologic areas of interest.

tor is then passed to our newly designed classification head, which consists of the following sequential layers:

- A linear layer that projects the 2560-dimensional input to a 256-dimensional space, acting as a feature bottleneck to condense information.
- A SiLU (Sigmoid-weighted Linear Unit) activation function to introduce nonlinearity, allowing the model to learn more complex decision boundaries.
- A dropout layer with a rate of 0.5, which randomly deactivates neurons during training to effectively mitigate overfitting.
- A final linear output layer that maps the 256-dimensional features to the 9 target class logits, producing the final predictions.

3 Experiments

3.1 Dataset

No external unlabeled pathology dataset was used, all operations in this paper were performed on the labeled BraTS-Path dataset [1,4], provided by the official BraTS 2025 challenge [10]. which consists of H&E-stained Formalin-Fixed,

Paraffin-Embedded (FFPE) tissue sections from the TCGA-GBM and TCGA-LGG collections. The data have been reclassified according to updated World Health Organization (WHO) criteria, focusing on glioblastoma cases. Expert annotations segment the slides into patches representing distinct histological regions. The dataset [1,10] covers nine histological categories:

- 1. Presence of cellular tumor (CT)
- 2. Pseudopalisading necrosis (PN)
- 3. Areas abundant in microvascular proliferation (MP)
- 4. Geographic necrosis (NC)
- 5. Infiltration into the cortex (IC)
- 6. Penetration into white matter (WM)
- 7. Leptomeningial infiltration (LI)
- 8. Regions with dense macrophages (DM)
- 9. Presence of lymphocytes (PL)

Figure 3 provides a qualitative overview of the dataset with representative images from each of the nine classes. The dataset is highly unbalanced, exhibiting a long-tailed class distribution as quantitatively detailed in Figure 4.

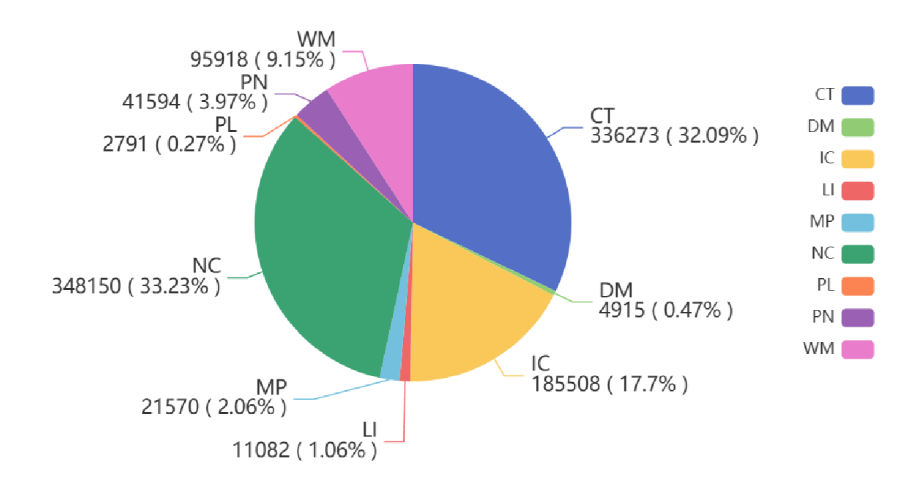


Fig. 4. Class distribution of the dataset, detailing the number and percentage of samples for each category.

3.2 Data pre-processing

Histopathological patches were input data from nine classes. To ensure uniform input for training and evaluation and ensure the generalization ability of the model, all input images were transformed using a pre-processing pipeline implemented via:

- Resize: All images were resized to a fixed size(resolution) of 224×224 pixels, ensuring uniform spatial dimensions of inputs.
- **ToTensor**: Images were converted into PyTorch tensors, scaling pixel values to the [0,1] range and rearranging the channel order to (C, H, W).
- Normalization: Pixel intensities were normalized using ImageNet statistics with mean [0.485, 0.456, 0.406] and standard deviation [0.229, 0.224, 0.225], which facilitates convergence during training process.

3.3 Evaluation Metrics

Let TP, TN, FP, and FN denote true positives, true negatives, false positives, and false negatives. The evaluation metrics used are defined as follows:

$$Accuracy = \frac{TP + TN}{TP + TN + FP + FN} \tag{1}$$

$$Precision = \frac{TP}{TP + FP} \tag{2}$$

$$Recall = \frac{TP}{TP + FN} \tag{3}$$

$$F1-Score = \frac{2 \cdot Precision \cdot Recall}{Precision + Recall}$$
(4)

Specificity =
$$\frac{TN}{TN + FP}$$
 (5)

$$MCC = \frac{TP \cdot TN - FP \cdot FN}{\sqrt{(TP + FP)(TP + FN)(TN + FP)(TN + FN)}}$$
(6)

A confusion matrix $C \in \mathbb{R}^{K \times K}$ was also used, where C_{ij} represents the proportion of samples from class i predicted as class j, and K is the number of classes. All metrics were computed on the validation set.

3.4 Experiment Settings

A 5-fold stratified cross-validation [5] scheme was used to evaluate model generalizability. Let $\mathcal{D}_f^{\mathrm{val}}$ denote the validation sets for fold f, and let \mathcal{M}_f be the model trained after fold f. The final performance metrics were obtained by averaging over the 5 validation folds:

$$Metric_{avg} = \frac{1}{5} \sum_{f=1}^{5} Metric(\mathcal{M}_f, \mathcal{D}_f^{val})$$

For each fold, we utilized the Adam optimizer with an initial learning rate of $1e^{-5}$ and a weight decay of 0.01. To ensure stable convergence, the learning rate

schedule included a one-epoch warmup followed by a cosine annealing scheduler, reducing the learning rate to a minimum of $1e^{-6}$. All models were trained on 4 NVIDIA V100 GPUs using a batch size of 256 and FP16 mixed-precision for computational efficiency.

4 Results

4.1 Local Validation

The model's performance was first evaluated on the local validation set using a 5-fold cross-validation methodology. A summary of key performance metrics for each class is provided in Table 1. The results show a wide range of performance across classes. High-performing classes, such as NC, were identified with exceptional reliability, achieving scores above 95% for all metrics. Moderately performing classes like IC and CT scored around 90%, though CT exhibited lower precision (0.86) while IC had a comparatively low recall (0.82). For the remaining classes, while overall accuracy remained high, their recall and F1-scores were significantly lower, a trend particularly pronounced for LI, DM, and PL.

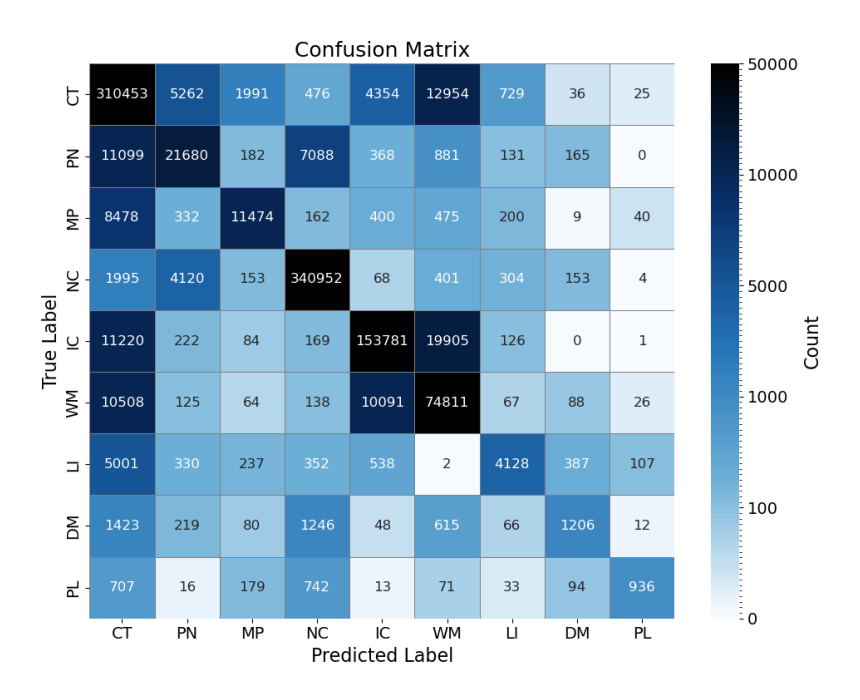


Fig. 5. Aggregated confusion matrix from the 5-fold cross-validation on the local validation set.

Table 1. The class-wise performance on the local validation set. We calculate the micro average of different metrics.

Metric	-	PN								Average
Accuracy										
Precision										l
										0.8775
Specificity										
F1	0.8906	0.5867	0.6372	0.9749	0.8660	0.7262	0.4895	0.3420	0.4749	0.8775
MCC	_	_	_	_	_	_	_	_	_	0.8347

A deeper analysis of these results was conducted using the aggregated confusion matrix from all five folds, visualized in Figure 5. The matrix reveals that CT, the majority class, is a primary source of confusion. The high concentration of false positives in its column indicates that samples from other classes are frequently misclassified as CT, which directly explains its lower precision. In contrast, NC, despite being the second-largest class, shows highly discriminative performance with minimal confusion.

The most notable trend is the model's difficulty with minority classes. The low recall values for LI, DM, and PL correspond directly to their small sample sizes in the dataset, confirming that the model struggles to learn their features and correctly identify them. Furthermore, the confusion matrix highlights other specific error patterns, such as the tendency for WM and IC to be misclassified as one another.

4.2 Online Validation and Test Resluts

The model's evaluation results, presented in Table 2, reveal a significant performance degradation when moving from the local to the online validation set. The model performed exceptionally well on the local data, achieving uniform scores of 0.8787 across Accuracy, Precision, Recall, and F1, with a corresponding MCC of 0.825. However, on the online validation set, these metrics declined sharply to 0.7677, with the F1-score reaching 0.5330 ± 0.036 and the MCC decreasing to 0.65087 ± 0.006 . Such a marked discrepancy between the two validation environments is indicative of poor generalization and suggests a significant degree of overfitting.[6].

Table 2. Online validation and test results.

	Accuracy	Precision	Recall	Specificity	F1	MCC
Validation set	0.76766	0.76766	0.76766			1 1
Test set	N/A	N/A	N/A	N/A	0.53301	0.65087

5 Conclusion

In this work, we presented a deep learning approach for the classification of glioblastoma histopathological subtypes by fine-tuning a pre-trained Virchow2 Vision Transformer. Our model demonstrated strong performance on a local validation set, achieving an F1-score of 0.8775 and an MCC of 0.8347, establishing it as a robust baseline for this complex classification task. The analysis revealed high accuracy for well-represented classes like Cellular Tumor (CT) and Necrosis (NC) but highlighted challenges with minority classes, which were often misclassified due to significant data imbalance.

In the BraTS-Pathology 2025 Challenge, our model achieved a second-place finish. It obtained an F1-score of 0.7676 and an MCC of 0.7064 on the Synapse online validation set, which decreased to 0.5330 and 0.6509, respectively, on the final test set. This performance discrepancy suggests that the model overfitted to the validation data, revealing a generalization gap. To address this, our future work will prioritize improving generalization by implementing advanced data augmentation and regularization strategies. Furthermore, we will investigate techniques specifically designed for long-tailed distributions to boost performance on less frequent histological classes.

Acknowledgements

This work was supported by Ningbo Major Science & Technology Project under Grant 2022Z126. (Corresponding: Ying Weng.)

References

- Bakas, S., Thakur, S.P., Faghani, S., Moassefi, M., Baid, U., Chung, V., Pati, S., Innani, S., Baheti, B., Albrecht, J., Karargyris, A., Kassem, H., Nasrallah, M.P., Ahrendsen, J.T., Barresi, V., Gubbiotti, M.A., López, G.Y., Lucas, C.H.G., Miller, M.L., Cooper, L.A.D., Huse, J.T., Bell, W.R.: Brats-path challenge: Assessing heterogeneous histopathologic brain tumor sub-regions (2024), https://arxiv. org/abs/2405.10871
- Darcet, T., Oquab, M., Mairal, J., Bojanowski, P.: Vision transformers need registers (2024), https://arxiv.org/abs/2309.16588
- 3. Dosovitskiy, A., Beyer, L., Kolesnikov, A., Weissenborn, D., Zhai, X., Unterthiner, T., Dehghani, M., Minderer, M., Heigold, G., Gelly, S., Uszkoreit, J., Houlsby, N.: An image is worth 16x16 words: Transformers for image recognition at scale. CoRR abs/2010.11929 (2020), https://arxiv.org/abs/2010.11929
- 4. Karargyris, A., Umeton, R., Sheller, M.J., Aristizabal, A., George, J., Wuest, A., Pati, S., Kassem, H., Zenk, M., Baid, U., Narayana Moorthy, P., Chowdhury, A., Guo, J., Nalawade, S., Rosenthal, J., Kanter, D., Xenochristou, M., Beutel, D.J., Chung, V., Bergquist, T., Eddy, J., Abid, A., Tunstall, L., Sanseviero, O., Dimitriadis, D., Qian, Y., Xu, X., Liu, Y., Goh, R.S.M., Bala, S., Bittorf, V., Puchala, S.R., Ricciuti, B., Samineni, S., Sengupta, E., Chaudhari, A., Coleman, C., Desinghu, B., Diamos, G., Dutta, D., Feddema, D., Fursin,

- G., Huang, X., Kashyap, S., Lane, N., Mallick, I., Mascagni, P., Mehta, V., Moraes, C.F., Natarajan, V., Nikolov, N., Padoy, N., Pekhimenko, G., Reddi, V.J., Reina, G.A., Ribalta, P., Singh, A., Thiagarajan, J.J., Albrecht, J., Wolf, T., Miller, G., Fu, H., Shah, P., Xu, D., Yadav, P., Talby, D., Awad, M.M., Howard, J.P., Rosenthal, M., Marchionni, L., Loda, M., Johnson, J.M., Bakas, S., Mattson, P., Consortium, F., Consortium, B., Consortium, A.: Federated benchmarking of medical artificial intelligence with medperf. Nature Machine Intelligence 5(7), 799–810 (2023). https://doi.org/10.1038/s42256-023-00652-2, https://doi.org/10.1038/s42256-023-00652-2
- Kohavi, R.: A study of cross-validation and bootstrap for accuracy estimation and model selection. In: Proceedings of the 14th International Joint Conference on Artificial Intelligence - Volume 2. p. 1137–1143. IJCAI'95, Morgan Kaufmann Publishers Inc., San Francisco, CA, USA (1995)
- Lin, T.Y., Goyal, P., Girshick, R., He, K., Dollár, P.: Focal loss for dense object detection (2018), https://arxiv.org/abs/1708.02002
- Neidlinger, P., Lenz, T., Foersch, S., Loeffler, C.M.L., Clusmann, J., Gustav, M., Shaktah, L.A., Langer, R., Dislich, B., Boardman, L.A., French, A.J., Goode, E.L., Gsur, A., Brezina, S., Gunter, M.J., Steinfelder, R., Behrens, H.M., Röcken, C., Harrison, T., Peters, U., Phipps, A.I., Curigliano, G., Fusco, N., Marra, A., Hoffmeister, M., Brenner, H., Kather, J.N.: A deep learning framework for efficient pathology image analysis (2025), https://arxiv.org/abs/2502.13027
- 8. Oquab, M., Darcet, T., Moutakanni, T., Vo, H., Szafraniec, M., Khalidov, V., Fernandez, P., Haziza, D., Massa, F., El-Nouby, A., Assran, M., Ballas, N., Galuba, W., Howes, R., Huang, P.Y., Li, S.W., Misra, I., Rabbat, M., Sharma, V., Synnaeve, G., Xu, H., Jegou, H., Mairal, J., Labatut, P., Joulin, A., Bojanowski, P.: Dinov2: Learning robust visual features without supervision (2024), https://arxiv.org/abs/2304.07193
- Piana, D., Iavarone, F., De Paolis, E., Daniele, G., Parisella, F., Minucci, A., Greco, V., Urbani, A.: Phenotyping tumor heterogeneity through proteogenomics: Study models and challenges. International Journal of Molecular Sciences 25(16) (2024). https://doi.org/10.3390/ijms25168830
- Synapse: Brain tumor pathology dataset (2025), https://www.synapse.org/ Synapse:syn64153130/wiki/631458, accessed: 2025-07-10
- Wang, X., Yang, S., Zhang, J., Wang, M., Zhang, J., Yang, W., Huang, J., Han, X.: Transformer-based unsupervised contrastive learning for histopathological image classification. Medical Image Analysis 81, 102559 (2022). https://doi.org/https://doi.org/10.1016/j.media.2022.102559, https://www.sciencedirect.com/science/article/pii/S1361841522002043
- 12. Zhang, X., Zhang, W., Cao, W.D., Cheng, G., Zhang, Y.Q.: Glioblastoma multiforme: Molecular characterization and current treatment strategy (review). Experimental and Therapeutic Medicine 3(1), 9 14 (2012). https://doi.org/10.3892/etm.2011.367
- Zimmermann, E., Vorontsov, E., Viret, J., Casson, A., Zelechowski, M., Shaikovski, G., Tenenholtz, N., Hall, J., Klimstra, D., Yousfi, R., Fuchs, T., Fusi, N., Liu, S., Severson, K.: Virchow2: Scaling self-supervised mixed magnification models in pathology (2024), https://arxiv.org/abs/2408.00738